An Evaluation of Scatterometer-Derived Oceanic Surface Pressure Fields

JÉRÔME PATOUX
Department of Atmospheric Sciences, University of Washington, Seattle, Washington

RALPH C. FOSTER
Applied Physics Laboratory, Seattle, Washington

ROBERT A. BROWN
Department of Atmospheric Sciences, University of Washington, Seattle, Washington

(Manuscript received 4 January 2007, in final form 27 June 2007)

ABSTRACT

Oceanic surface pressure fields are derived from the NASA Quick Scatterometer (QuikSCAT) surface wind vector measurements using a two-layer similarity planetary boundary layer model in the midlatitudes and a mixed layer planetary boundary layer model in the tropics. These swath-based surface pressure fields are evaluated using the following three methods: 1) a comparison of bulk pressure gradients with buoy pressure measurements in the North Pacific and North Atlantic Oceans, 2) a least squares difference comparison with the European Centre for Medium-Range Weather Forecasts (ECMWF) surface pressure analyses, and 3) a parallel spectral analysis of the QuikSCAT and ECMWF surface pressure fields. The correlation coefficient squared between scatterometer-derived pressure fields and buoys is found to be $R^2 = 0.936$. The average root-mean-square difference between the scatterometer-derived and the ECMWF pressure fields ranges from 1 to 3 hPa, depending on the latitude and season, and decreases after the assimilation of QuikSCAT winds in the ECMWF numerical weather prediction model. The spectral components of the scatterometer-derived pressure fields are larger than those of ECMWF surface analyses at all scales in the midlatitudes and only at shorter wavelengths in the tropics.

1. Introduction

Surface wind vector measurements that cover over 90% of the ice-free world's oceans on a daily basis are available now routinely from the National Aeronautics and Space Administration (NASA) Quick Scatterometer (QuikSCAT; or QS) satellite scatterometer. This mission followed the European Remote Sensing satellite *ERS-1* (1991–95) and *ERS-2* (1995–present) scatterometers and the NASA Scatterometer (NSCAT) (1996–97). The QS has provided an almost continuous stream of measurements since July 1999. The surface wind measurements from all of these satellites have had a profound effect on research and applications in meteorology and oceanography (Milliff et al. 2002; Liu 2002). An application of interest to meteorologists in general, and weather forecasters in particular, is the ability to compute a surface pressure field from satellite wind measurements (Von Ahn et al. 2006a,b).

Such surface pressure fields present the following four main advantages: 1) They integrate the scatterometer data into a scalar field that is often simpler to analyze and interpret than the thousands of wind vectors constituting a swath of scatterometer measurements. 2) Surface pressure is a valuable quantity in forecasting the weather that allows for quick identification of the position of low pressure centers and fronts in midlatitude storms. 3) The intensity of storms and fronts consistent with the scatterometer wind vectors is readily apparent in the spacing of the surface isobars. 4) The retrieved surface pressure field is inherently smoother than the surface wind vector field and can be used to filter wind direction retrieval errors caused by rain contamination and sampling geometry, as well as random errors (Patoux and Brown 2001a).

Various schemes have been designed to compute surface pressure fields from wind vectors (Brown and Levy

Corresponding author address: Jérôme Patoux, Department of Atmospheric Sciences, University of Washington, 408 ATG Building, Box 351640, Seattle, WA 98195-1640.
E-mail: jerome@atmos.washington.edu

DOI: 10.1175/2007JAMC1683.1

1986; Harlan and O'Brien 1986; Hsu et al. 1997; Hsu and Liu 1996; Zierden et al. 2000; Hilburn et al. 2003). Oceanic surface pressure fields derived from scatterometer wind measurements using the University of Washington (UW) planetary boundary layer (PBL) model have been used to evaluate numerical weather prediction (NWP) model analyses in the Southern Hemisphere (Levy and Brown 1991), to estimate the central pressure of midlatitude storms (Brown and Zeng 1994), and to identify a low bias in the *ERS-1*/*-2* scatterometer model function for wind retrievals above $\approx$20 m s^{-1} (Foster and Brown 1994; Brown 1998, 2000; Zeng and Brown 1998; Brown and Zeng 2001). The oceanic surface pressure fields derived from QS wind measurements (hereinafter referred to as the UWQS pressure fields) have been used to study the development of frontal waves over the Southern Ocean (Patoux et al. 2005) and are used in near–real time (NRT) at the National Oceanic and Atmospheric Administration's (NOAA's) Ocean Prediction Center (OPC; Von Ahn et al. 2006a,b). The NOAA OPC weather forecasters overlay the UWQS surface pressure fields with other observational fields and NWP model outputs to ensure that the sea level pressure analyses and short-term wind warnings to the marine community are consistent with each other and with the QS winds. The UWQS pressure fields agree with ship and buoy observations most of the time, and, in many cases, are found to yield lower central pressures in midlatitude cyclones than either the OPC manual analyses or the Global Forecast System (GFS) pressure fields (see also Chelton et al. 2006).

The UWQS pressure fields are archived (online at http://pbl.atmos.washington.edu),[1] and are available for meteorological and oceanographic applications. The present study uses three methodologies to evaluate these swath-based oceanic surface pressure fields covering most of the existing QS period (from July 1999 to December 2005). We first compare the pressure differences between pairs of buoys with those calculated from UWQS. Second, we examine the rms difference between UWQS and European Centre for Medium Range Weather Forecasting (ECMWF) surface analyses. Third, we compare the spectral variance of the UWQS pressures with that from ECMWF.

2. Data

We use the L2B QS surface wind vectors distributed by the Jet Propulsion Laboratory (JPL) Physical Oceanography Distributed Active Archive Center (PODAAC) after removal of those wind vector measurements that have been contaminated by rain (Huddleston and Stiles 2000) and/or ice. Milliff et al. (2004) have shown that the rain flag may be too conservative and that omitting all of the rain-flagged vectors can bias estimates of derivative quantities, such as the wind stress curl. However, the surface pressure patterns obtained from scatterometer winds are relatively insensitive to localized patches of either missing or erroneous vectors, so we have applied the rain flag as recommended by PODAAC. The L2B winds are provided in swaths that are 1600 km wide, with an approximate spacing of 25 km. We use the selected vector out of the up-to-four possible ambiguous vectors. The pressure retrieval methodology is generally insensitive to the small number ($<$5%) of incorrectly selected ambiguities in the L2B product.

Buoy surface pressure measurements are obtained from the NOAA National Data Buoy Center (NDBC) in the form of hourly reports. They have a precision of 0.1 hPa and an accuracy of 1 hPa (information online at http://ndbc.noaa.gov/rsa.shtml).

We extract the sea level pressure, sea surface temperature (SST), 2-m air temperature (T_{air}), and 2-m humidity (Q_{air}) from the dataset ds111.1 ECMWF surface analyses obtained from the National Center for Atmospheric Research (NCAR). These analyses are output on a Gaussian (*n*80) grid with a resolution of about 1.125°. Both the L2B winds and the ds111.1 analyses are interpolated onto a 0.5° $\times$ 0.5° grid.

The monthly mean 925-hPa winds that are used to parameterize entrainment in the tropical mixed layer PBL model were obtained from the National Centers for Environmental Prediction (NCEP)–NCAR reanalysis (Kalnay et al. 1996). These data were provided by the NOAA/Office of Oceanic and Atmospheric Research (OAR)/Earth System Research Laboratory Physical Sciences Division, in Boulder, Colorado, from their Web site (http://www.cdc.noaa.gov/). The wind vectors, available on a 2.5° grid, were interpolated onto our 0.5° grid. Twelve monthly mean values were calculated at each grid point from the years 1948 to 2002.

3. Surface pressure retrieval from scatterometer winds

Retrieving pressure fields from surface wind measurements is a four-step process:

1) At each grid point of the midlatitude sections of the swath, the pressure gradient at the top of the boundary layer is estimated using a two-layer similarity PBL model, which includes the effects of stratification and a gradient wind correction.

[1] The archive will be updated for the duration of the QS mission.

2) At each grid point of the tropical section of the swath, the pressure gradient at the top of the boundary layer is estimated using a simple mixed layer PBL model that includes entrainment at the top of the PBL.
3) An optimal zero-mean surface pressure pattern is fit to the swath of pressure gradients by least squares minimization.
4) The absolute value of these relative pressures is set by anchoring the pressure pattern to either (a) one or several buoy pressure measurements when available, or (b) a surface pressure analysis provided by a NWP model. In this study we choose the second method and set the absolute values of pressure by matching the mean UWQS pressure to the mean ECMWF pressure for each swath. As we shall emphasize later, while the absolute values of the UWQS pressure are determined by matching the mean pressure, the pressure gradients are determined primarily by the scatterometer winds and the PBL models, modified by the stratification determined from SST, T_{air}, and Q_{air}.

Each of these steps is now described in more detail. The complete derivation of the analytical solutions is detailed in Patoux (2004).

a. The midlatitude similarity model

The two-layer similarity model used in the midlatitudes, referred to as the UW PBL inverse model in the literature, has been extensively documented (Brown and Levy 1986; Brown and Liu 1982; Brown and Zeng 1994; Patoux 2004) and will be only briefly summarized here. At each point of a swath or grid where a surface wind vector is available, the PBL wind profile is approximated by patching a stratification-dependent Ekman layer solution to a stratification-dependent surface layer. Including stratification requires SST, T_{air}, and Q_{air}, which we obtain from the ECMWF surface analyses at the closest synoptic time.

At the top of this PBL wind profile, we initially assume the flow to be in geostrophic balance. In natural coordinates the pressure gradient normal to the direction of the flow is estimated as

$$\frac{1}{\rho}\frac{\partial P}{\partial n} = fV_g, \tag{1}$$

where f is the Coriolis parameter, ρ is the density, P is the atmospheric pressure, V_g is the geostrophic wind speed, and n is the normal coordinate. Once a swath of pressure gradients is calculated and a pressure field is fit to the gradients by least squares minimization (see section 3c below), the radius of curvature R is estimated (Patoux and Brown 2002; Endlich 1961). The field of R is smoothed to avoid spuriously small curvature estimates. We then assume the flow to be in gradient wind balance at each grid point as

$$\frac{1}{\rho}\frac{\partial P}{\partial n} = fV_g = fV\left(1 + \frac{V}{fR}\right), \tag{2}$$

which modifies the estimates of the pressure gradients. The resulting grid of pressure gradients are the midlatitude inputs to the least squares fit described in section 3c.

b. The tropical mixed layer model

In the tropics we use the simple model described in Patoux et al. (2003), which is based on the mixed layer model by Stevens et al. (2002). The steady-state balance equations of motion are integrated over the depth h of the boundary layer to yield the following momentum integral:

$$f\mathbf{k} \times \mathbf{U} + \frac{1}{\rho_0}\nabla P = \frac{\boldsymbol{\tau}(h) - \boldsymbol{\tau}(0)}{h}, \tag{3}$$

where $\mathbf{U} = (U, V)$ and P are the boundary layer–averaged wind and pressure, respectively, and $\boldsymbol{\tau}(0)$ and $\boldsymbol{\tau}(h)$ are the turbulent stresses at the bottom and top of the boundary layer. The surface stress τ_0 is calculated using the neutral equivalent 10-m surface wind vector provided by the scatterometer and the drag coefficient described in Brown and Liu (1982).

We parameterize the entrainment flux as

$$\boldsymbol{\tau}(h) = w_e \Delta\mathbf{U} = w_e(\mathbf{U}_T - \mathbf{U}), \tag{4}$$

where $\mathbf{U}_T = (U_T, V_T)$ is the wind above the boundary layer. In this paper we use a monthly climatology of $\mathbf{U}_T$ calculated from the NCEP–NCAR reanalysis 925-hPa winds. A mean value of h = 500 m is used for h and w_e = 0.01 m s^{-1} is the entrainment velocity. The insensitivity of the pressure retrievals to the ratio (w_e/h) is discussed in Patoux et al. (2003). The pressure gradient is obtained by iterative integration of the wind profile (3).

c. The least squares pressure fit

The two-layer similarity model and the mixed layer model yield three sets of zonal (P_x) and meridional (P_y) pressure gradients: two in the midlatitudes (from 70° to 10°S and from 10° to 70°N) and one in the tropics (from 20°S to 20°N). For continuity and smoothness they are blended between 10° and 20° in each hemisphere as described in Patoux et al. (2003) to yield a single grid of pressure gradients.

At each point of the resulting grid, we can write, in matrix notation (Brown and Zeng 1994),

$$\mathbf{HP} = \mathbf{P_g} \quad \text{where} \quad \mathbf{H} \equiv \left| \begin{matrix} \dfrac{1}{a\cos\phi}\dfrac{\partial}{\partial\lambda} \\ \dfrac{1}{a}\dfrac{\partial}{\partial\phi} \end{matrix} \right. \quad \text{and} \quad \mathbf{P_g} \equiv \left| \begin{matrix} P_x \\ P_y \end{matrix} \right. , \tag{5}$$

where a is the radius of the earth, λ is the longitude, and ϕ is the latitude. The least squares best estimate for the pressure field $\mathbf{P}$ is obtained by solving

$$\mathbf{H}^{\mathrm{T}}\mathbf{HP} - \mathbf{H}^{\mathrm{T}}\mathbf{P_g} = 0. \tag{6}$$

Least squares minimization tends to distribute the error globally, so the estimate of $\mathbf{P}$ is relatively insensitive to localized errors in the vector surface winds, which is the most common pattern of error in the ambiguity selection once the rain-flagged vectors have been removed. Because the L2B wind vectors were originally interpolated onto a 0.5° × 0.5° grid, the solution pressure field $\mathbf{P}$ has a 0.5° grid spacing.

d. *The pressure anchor*

The solution matrix $\mathbf{P}$ defines a grid of zero-mean relative pressure values. In regions of the ocean where in situ (typically buoy or ship) pressure measurements are available, absolute values of pressure are obtained by anchoring the pressure field $\mathbf{P}$ to a surface pressure measurement or to several buoy measurements. In this second case, the pressure anchor is the mean difference between the pressure field $\mathbf{P}$ and the buoy measurements.

In regions of the ocean where in situ measurements are not available, the absolute values of the pressure are obtained by minimizing the difference between the solution $\mathbf{P}$ and an NWP surface pressure analysis. In this study we generate surface pressure swaths that include regions of the ocean where buoy and ship observations are scarce. We therefore anchor each pressure field to the closest-in-time ECMWF surface pressure analysis in a mean sense, which implies a maximum time difference of 3 h between the analysis and the UWQS swath. It is important to note that the pressure anchor only affects the mean value of the solution $\mathbf{P}$, and not its structure.

4. Comparison with buoys

The UWQS oceanic surface pressure fields are first compared with measurements of surface pressure by NDBC buoys. Because we are interested in evaluating the pressure gradient structure of the UWQS fields, we identify QS swaths that pass over *two* buoys, as illustrated in Fig. 1 for buoys 46001 and 51001, and calculate the pressure difference between the two buoys, which can be thought of as an integrated pressure gradient, or bulk pressure gradient (BPG). We then compare the buoy BPG with the corresponding BPG in the UWQS swath. In this example, the buoy BPG is 33.2 hPa and the UWQS BPG is 33.9 hPa. We repeated this comparison for the 1362 such swaths that cover these two buoys over the 7-yr QS period. The results are summarized in Fig. 2a. The correlation coefficient squared is $R^2 = 0.941$, the y intercept $a = -0.4 \pm 0.3$, and the slope $b = 1.083 \pm 0.014$, which shows that the UWQS BPG tends to be somewhat stronger than that observed.

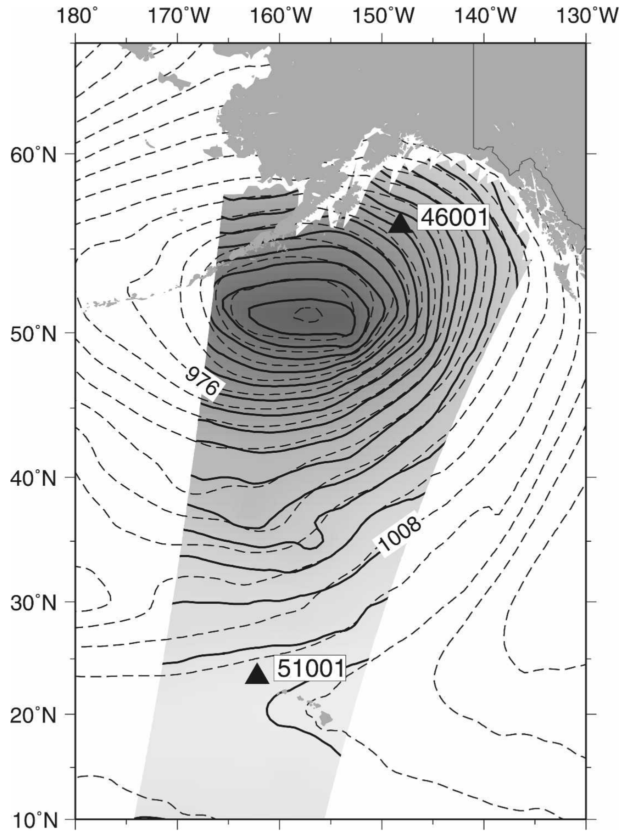

FIG. 1. Example of buoy-swath geometry for bulk pressure gradient comparisons. UWQS, at about 0500 UTC (solid lines) and ECMWF analysis, at 0600 UTC (dashed lines) 8 Mar 2005; and NDBC buoys (triangles) are shown. Contour interval is 4 hPa.

Figure 1 also shows the ECMWF surface pressure analysis at the closest synoptic time (dashed lines). For comparison, each ECMWF BPG is similarly calculated (34.6 hPa in this example) and the correlation between buoy BPG and ECMWF BPG is computed over the same 1362 collocations ($R^2 = 0.995$, y intercept $a = -0.1 \pm 0.1$, slope $b = 0.982 \pm 0.004$; see Fig. 2b). The correlation is very high because buoy measurements

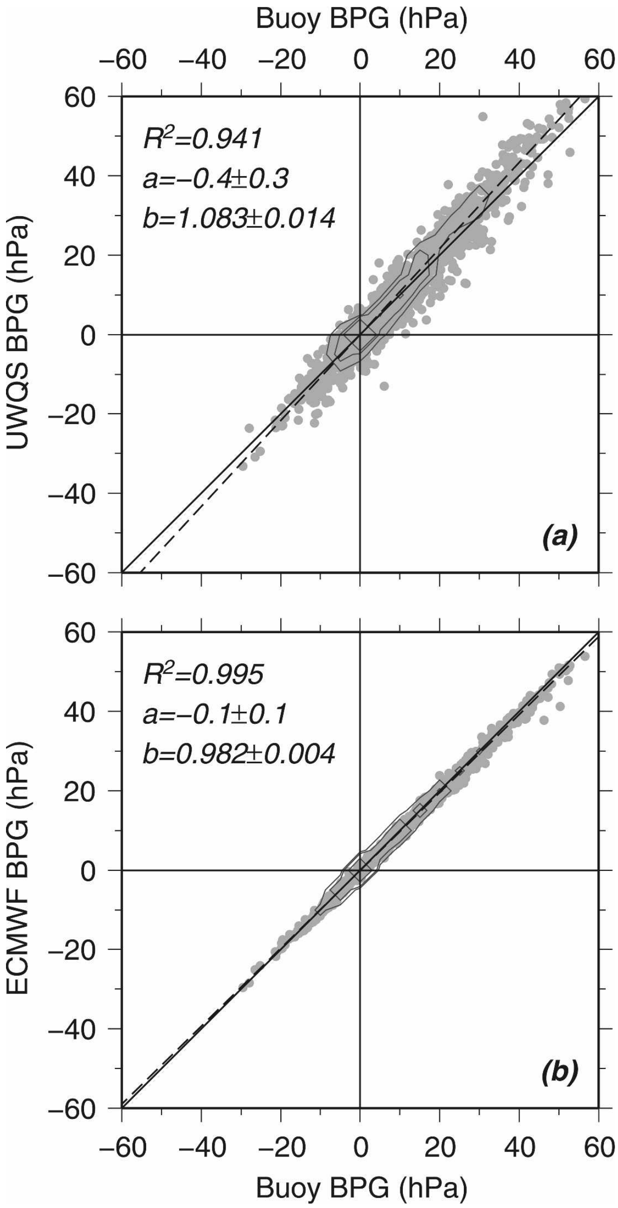

FIG. 2. Comparison of buoy, ECMWF, and UWQS BPG between NDBC buoys 46001 and 51001. The contours contain 25%, 50%, and 75% of the data points respectively.

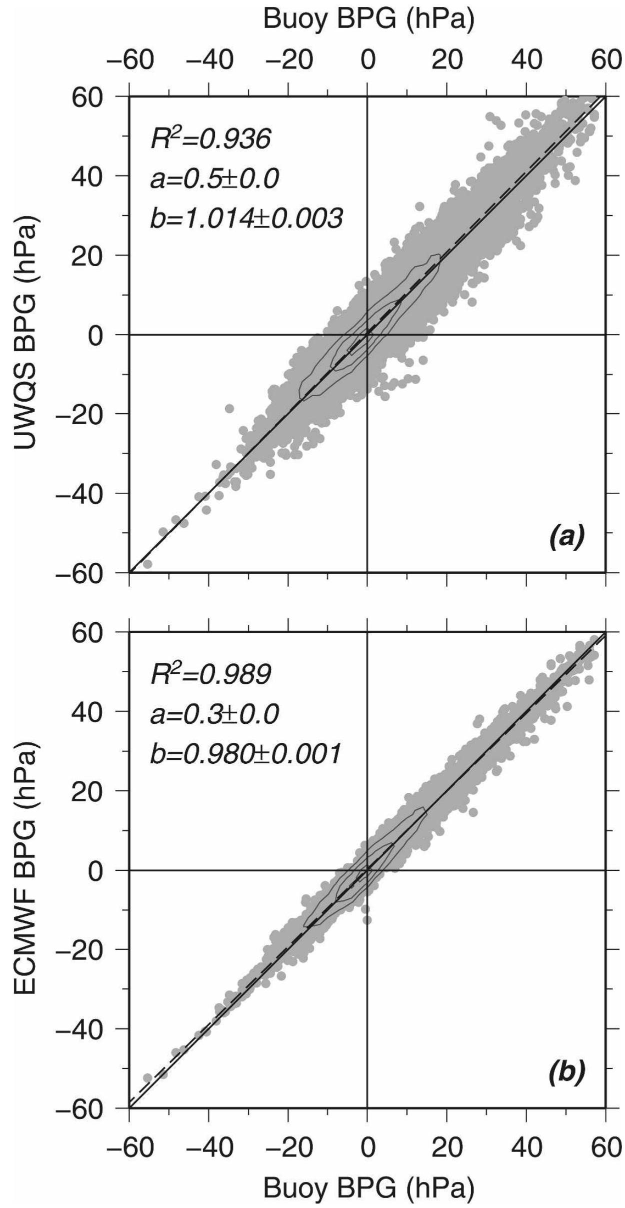

FIG. 3. As in Fig. 2, but for all buoys.

are assimilated into the ECMWF analyses. The UWQS BPGs obtained from scatterometer winds, however, use no buoy pressure measurements (although they do include stratification based on ECMWF SST, T_{air}, and Q_{air}). An ideal comparison between UWQS and ECMWF would use buoy measurements that are not assimilated in the ECMWF NWP model, so the comparison with the ECMWF correlations is only provided as a reference. Considering that the UW PBL model has no knowledge of the buoy measurements, a correlation of 0.941 shows that the pressure retrieval scheme is able to reproduce buoy pressure differences of good quality from the scatterometer winds. This also reinforces the conclusions of Chelton et al. (2006) about the generally high quality of the QuikSCAT winds.

We applied the methodology described above to 52 buoy geometries using the NDBC buoys (shown below in Fig. 4). By varying the geometry we ensure that both ascending (≈0600 LT) and descending (≈1800 LT) swaths are sampled, as well as different geographical locations. The results are summarized in Fig. 3 and Table 1. Note that a smaller number of collocations was possible in the North Atlantic because of the longitudinal separation between buoys (i.e., the occurrence of

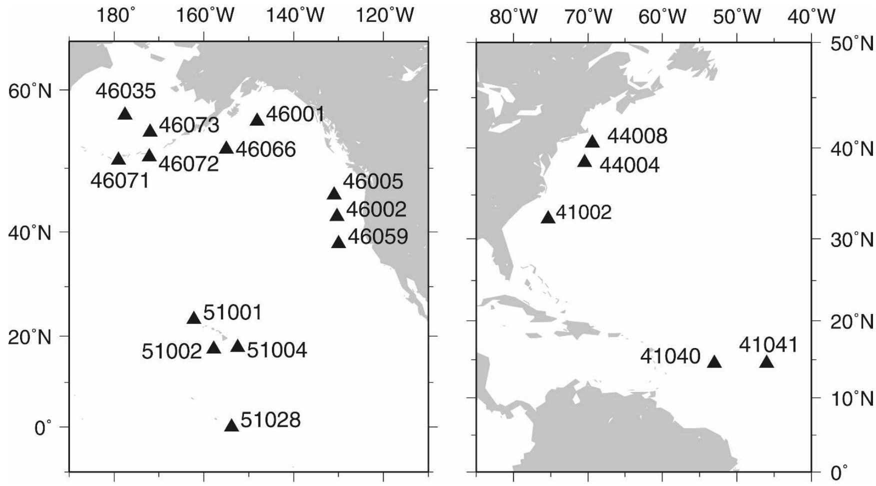

FIG. 4. Locations of the NDBC buoys used in the correlation calculations.

two buoys being intersected by the same swath is less common; see Fig. 4) and the lesser availability of NDBC measurements in this basin between 1999 and 2005 (i.e., measurement gaps). The correlation between buoy and UWQS BPG is $R^2 = 0.936$, with a slight positive bias toward stronger UWQS BPG (y intercept $a = 0.5 \pm 0.0$, slope $b = 1.014 \pm 0.003$).

The statistics are plotted as a function of distance between the two buoys in Fig. 5, where the results are further sorted by geographic region. Figure 5a shows that the correlations are overall independent of distance and are all greater than 0.9 in the Gulf of Alaska (black dots). The correlations involving buoy 51028 at the equator are slightly weaker (open circles), which suggests that the mixed layer model used to calculate pressure gradients in the tropical regions is a relatively poorer approximation to the real flow than the similarity model in the midlatitudes. The correlations are notably weaker in the North Atlantic (open triangles): three of the buoys are in the vicinity of the Gulf Stream, where SST and T_{air} variability is large and both stratification and baroclinic effects on the PBL mean flow can be strong (Foster et al. 1999; Brown and Liu 1982). The lower BPG correlations for pairs including these buoys may be the result of errors in the ECMWF surface temperatures and/or the lack of thermal wind effects in the UWQS pressures. They may also be due to errors in the scatterometer winds caused by ocean currents, which translate into errors in the retrieved pressure fields. Kelly et al. (2001) showed that differences of up to 1 m s^{-1} between scatterometer and buoy winds could be due to strong ocean currents. The correlations around Hawaii (open squares) are significantly weaker. Note that there is a big QS data gap resulting from the islands and that both the ocean surface roughness and the PBL dynamics can be strongly influenced by the topography, making the pressure retrieval more challenging than over the open ocean. Interestingly, the ECMWF correlations are weaker as well in that region.

The correlations suggest that the pressure retrieval scheme is affected by (a) data gaps in the scatterometer measurements; (b) poor characterization of the SST and T_{air}, and therefore stratification and baroclinicity; and/or (c) incomplete parameterizations in the two PBL models used in the retrieval. There are several limitations to both models. In the tropics we use a constant PBL height $h = 500$ m and $w_e = 0.01$ m s^{-1} and climatological $\mathbf{U}_T$. Although these approximations have yielded encouraging preliminary results (Stevens et al. 2002; Patoux et al. 2003), they clearly depart from the real instantaneous values. In the midlatitudes the gradient wind balance assumption above the PBL improves the UWQS pressure fields. However, a more accurate model will include nonlinear mean flow advection and baroclinicity, which can have first-order contributions to the PBL dynamics in the vicinity of fronts and low pressure centers. Yet, despite these limitations, a correlation of $R^2 = 0.936$ with buoy measurements suggests that the combination of the two PBL models with scatterometer winds is quite efficient at producing surface pressure fields over the ocean that correctly reproduce the observed BPGs over small and large distances.

5. Comparison with ECMWF pressure analyses

The UWQS surface pressure fields are now compared with ECMWF surface pressure analyses by calculating the root-mean-square (rms) difference between each UWQS swath and the closest-in-time ECMWF analysis. In the example shown in Fig. 1, the

TABLE 1. Summary of correlations between buoy, ECMWF, and UWQS BPG: correlation coef squared R^2, y intercept a, and slope b.

Buoy pair	R^2 (QS)	R^2 (EC)	a (QS)	a (EC)	b (QS)	b (EC)	Hits
			North Pacific Ocean				
46001–46002	0.966	0.985	-1.7 ± 0.7	0.3 ± 0.4	1.074 ± 0.037	0.964 ± 0.022	125
46001–46005	0.962	0.981	-1.0 ± 0.4	0.6 ± 0.3	1.065 ± 0.026	0.969 ± 0.017	254
46001–46059	0.955	0.990	-0.8 ± 0.3	0.0 ± 0.1	1.010 ± 0.013	0.981 ± 0.006	1168
46001–46066	0.965	0.983	-0.4 ± 0.1	-0.4 ± 0.1	1.013 ± 0.011	0.963 ± 0.007	1268
46001–51001	0.941	0.995	-0.4 ± 0.3	-0.1 ± 0.1	1.083 ± 0.014	0.982 ± 0.004	1436
46001–51002	0.939	0.994	0.3 ± 0.3	0.5 ± 0.1	1.076 ± 0.016	0.985 ± 0.005	1098
46001–51004	0.938	0.993	-0.2 ± 0.3	0.6 ± 0.1	1.071 ± 0.018	0.982 ± 0.005	930
46001–51028	0.941	0.994	1.8 ± 0.4	0.8 ± 0.1	1.044 ± 0.029	0.982 ± 0.008	326
46002–46059	0.935	0.948	0.5 ± 0.1	0.4 ± 0.1	0.998 ± 0.017	0.946 ± 0.014	946
46002–51028	0.868	0.981	4.0 ± 0.5	0.9 ± 0.2	1.054 ± 0.041	0.981 ± 0.014	388
46005–46002	0.929	0.923	-0.4 ± 0.1	-0.2 ± 0.1	0.973 ± 0.017	0.902 ± 0.017	942
46005–46059	0.937	0.960	0.0 ± 0.1	0.1 ± 0.1	1.007 ± 0.017	0.954 ± 0.012	956
46005–51004	0.915	0.985	1.8 ± 0.3	0.4 ± 0.1	1.053 ± 0.027	0.968 ± 0.010	559
46005–51028	0.881	0.982	3.2 ± 0.4	0.7 ± 0.1	1.041 ± 0.032	0.981 ± 0.011	589
46035–46071	0.938	0.941	-0.1 ± 0.2	0.2 ± 0.2	1.007 ± 0.024	0.935 ± 0.021	468
46035–46072	0.975	0.991	0.5 ± 0.1	0.9 ± 0.1	1.046 ± 0.011	1.000 ± 0.006	845
46035–46073	0.977	0.988	-0.3 ± 0.1	-0.0 ± 0.1	1.030 ± 0.022	0.984 ± 0.015	212
46035–51001	0.936	0.994	-0.1 ± 0.3	0.8 ± 0.1	1.036 ± 0.017	0.989 ± 0.005	1151
46035–51028	0.904	0.992	0.5 ± 0.3	1.4 ± 0.1	0.961 ± 0.020	0.986 ± 0.006	1028
46059–51028	0.848	0.976	4.2 ± 0.7	0.2 ± 0.2	1.118 ± 0.056	0.963 ± 0.018	293
46066–46035	0.980	0.998	1.2 ± 0.4	-0.0 ± 0.1	1.024 ± 0.022	0.981 ± 0.007	168
46066–46071	0.973	0.987	0.6 ± 0.9	-0.3 ± 0.6	0.994 ± 0.063	0.953 ± 0.042	31
46066–46072	0.981	0.994	1.8 ± 0.2	0.9 ± 0.1	1.042 ± 0.017	0.980 ± 0.009	292
46066–46073	0.988	0.998	-0.2 ± 0.4	-0.6 ± 0.2	1.022 ± 0.032	0.983 ± 0.014	51
46066–51001	0.951	0.993	0.6 ± 0.2	0.4 ± 0.1	1.084 ± 0.013	0.983 ± 0.005	1294
46066–51002	0.945	0.995	0.7 ± 0.3	0.8 ± 0.1	1.061 ± 0.018	0.987 ± 0.005	752
46066–51004	0.947	0.994	0.0 ± 0.4	0.9 ± 0.1	1.061 ± 0.023	0.981 ± 0.007	460
46066–51028	0.934	0.992	2.1 ± 0.4	1.2 ± 0.2	1.032 ± 0.036	0.979 ± 0.012	233
46071–46072	0.923	0.962	-0.1 ± 0.2	0.3 ± 0.1	0.811 ± 0.025	0.775 ± 0.016	353
46071–46073	0.922	0.954	-0.4 ± 0.3	-0.7 ± 0.2	0.911 ± 0.037	0.848 ± 0.026	202
46071–51001	0.911	0.984	-0.6 ± 0.8	0.0 ± 0.3	1.046 ± 0.040	1.020 ± 0.016	258
46071–51028	0.893	0.982	-0.0 ± 0.8	0.7 ± 0.3	1.005 ± 0.049	1.020 ± 0.020	196
46072–46073	0.956	0.987	-0.4 ± 0.2	-0.8 ± 0.1	1.060 ± 0.029	0.981 ± 0.014	239
46072–51001	0.959	0.997	-0.9 ± 0.9	-0.7 ± 0.2	1.008 ± 0.043	0.986 ± 0.011	92
46072–51002	0.950	0.991	-1.0 ± 0.3	-0.0 ± 0.1	1.022 ± 0.018	0.991 ± 0.007	637
46072–51028	0.928	0.991	0.0 ± 0.4	0.4 ± 0.1	0.995 ± 0.023	0.995 ± 0.008	554
46073–51001	0.955	0.999	-0.5 ± 1.9	-0.1 ± 0.3	0.979 ± 0.102	0.990 ± 0.015	21
46073–51004	0.949	0.991	-0.9 ± 0.6	0.7 ± 0.3	0.994 ± 0.037	0.990 ± 0.016	149
46073–51028	0.930	0.995	0.1 ± 0.6	1.0 ± 0.2	0.996 ± 0.044	0.995 ± 0.012	150
51001–51002	0.893	0.936	-0.5 ± 0.1	0.1 ± 0.1	0.985 ± 0.025	0.938 ± 0.018	691
51001–51004	0.889	0.930	-1.4 ± 0.1	0.0 ± 0.1	1.053 ± 0.037	0.918 ± 0.025	393
51001–51028	0.722	0.939	0.6 ± 0.8	0.0 ± 0.3	1.017 ± 0.095	0.931 ± 0.036	175
51002–51004	0.445	0.508	-0.7 ± 0.1	0.2 ± 0.0	0.685 ± 0.054	0.684 ± 0.048	7758
51002–51028	0.522	0.876	0.6 ± 0.5	-0.2 ± 0.2	0.941 ± 0.098	0.885 ± 0.036	330
51004–51028	0.519	0.885	1.5 ± 0.6	0.0 ± 0.2	0.953 ± 0.099	0.933 ± 0.036	341
			North Atlantic Ocean				
41040–41041	0.685	0.692	-0.5 ± 0.1	0.2 ± 0.1	0.972 ± 0.151	0.750 ± 0.114	78
44004–41002	0.777	0.964	1.4 ± 0.1	0.2 ± 0.0	1.012 ± 0.024	0.969 ± 0.008	2093
44004–41040	0.873	0.976	-1.4 ± 0.7	0.6 ± 0.3	0.937 ± 0.088	0.978 ± 0.038	69
44004–44008	0.706	0.901	-0.4 ± 0.1	0.1 ± 0.0	0.886 ± 0.031	0.881 ± 0.016	1316
44008–41002	0.790	0.975	1.7 ± 0.2	0.1 ± 0.0	1.021 ± 0.023	0.959 ± 0.007	2178
44008–41040	0.857	0.974	-1.1 ± 0.7	0.7 ± 0.3	0.935 ± 0.085	1.006 ± 0.037	82
44008–41041	0.752	0.977	-2.6 ± 1.4	1.0 ± 0.6	0.723 ± 0.188	1.053 ± 0.073	23
			Total				
Total	0.936	0.989	0.5 ± 0.0	0.3 ± 0.0	1.014 ± 0.003	0.980 ± 0.001	29 658

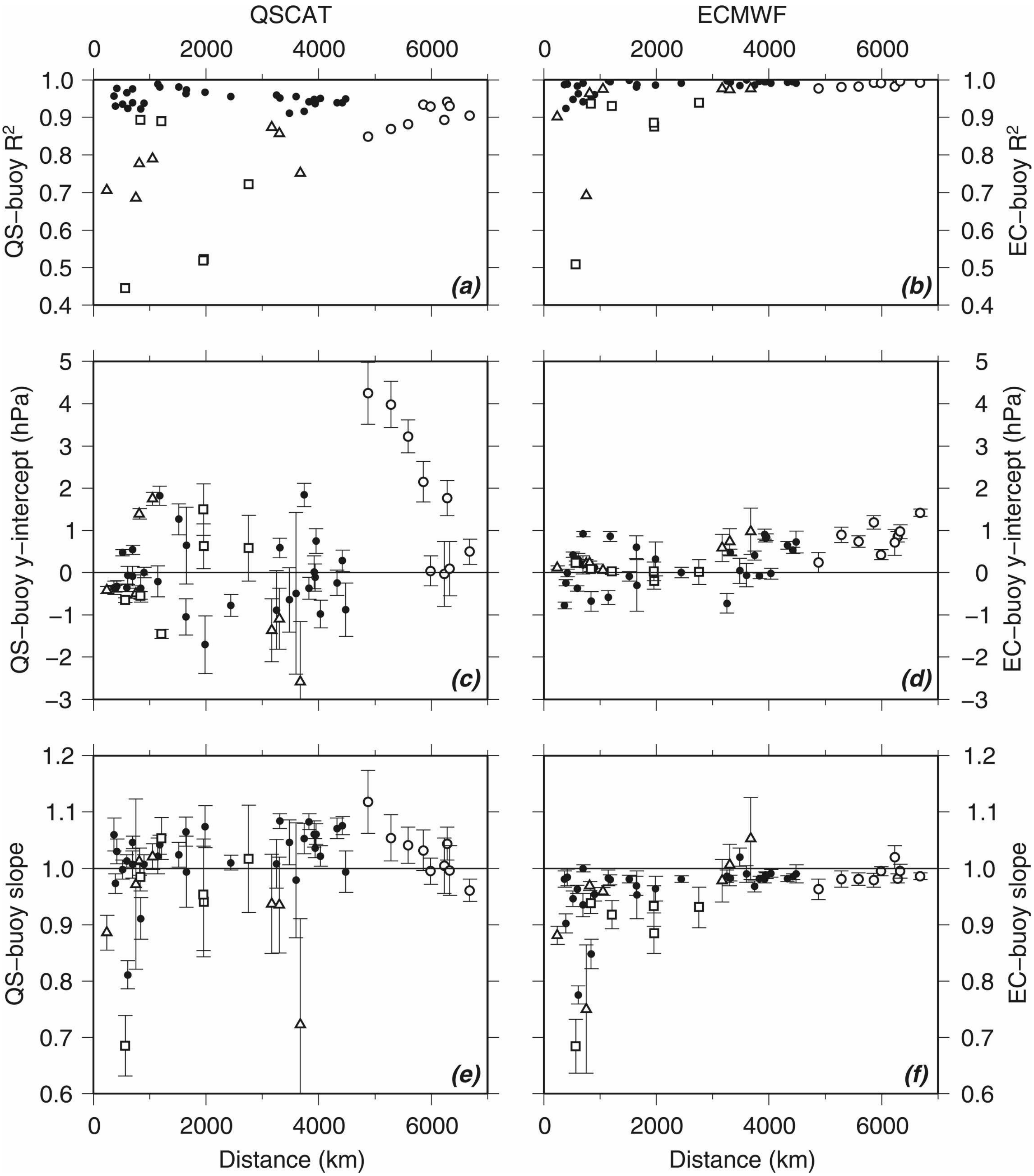

FIG. 5. BPG statistics as a function of the distance between buoys: (a) QS R^2, (b) ECMWF R^2, (c) QS y intercept, (d) ECMWF y intercept, (e) QS slope, and (f) ECMWF slope. Shown are buoy pairs containing buoy 51028 at the equator (open circles), buoy pairs in the Atlantic Ocean (triangles), buoy pairs across Hawaii (squares), and remaining buoys in the Gulf of Alaska (black dots).

rms difference over the entire swath is 2.4 hPa. The mean difference between the two pressure fields is forced to be zero, so we are comparing the differences in structure rather than the absolute values of pressure.

Because we use different PBL models in the midlatitudes and the tropics, and because we are interested in comparing the Northern and Southern Hemispheres, the rms difference is also calculated in the northern

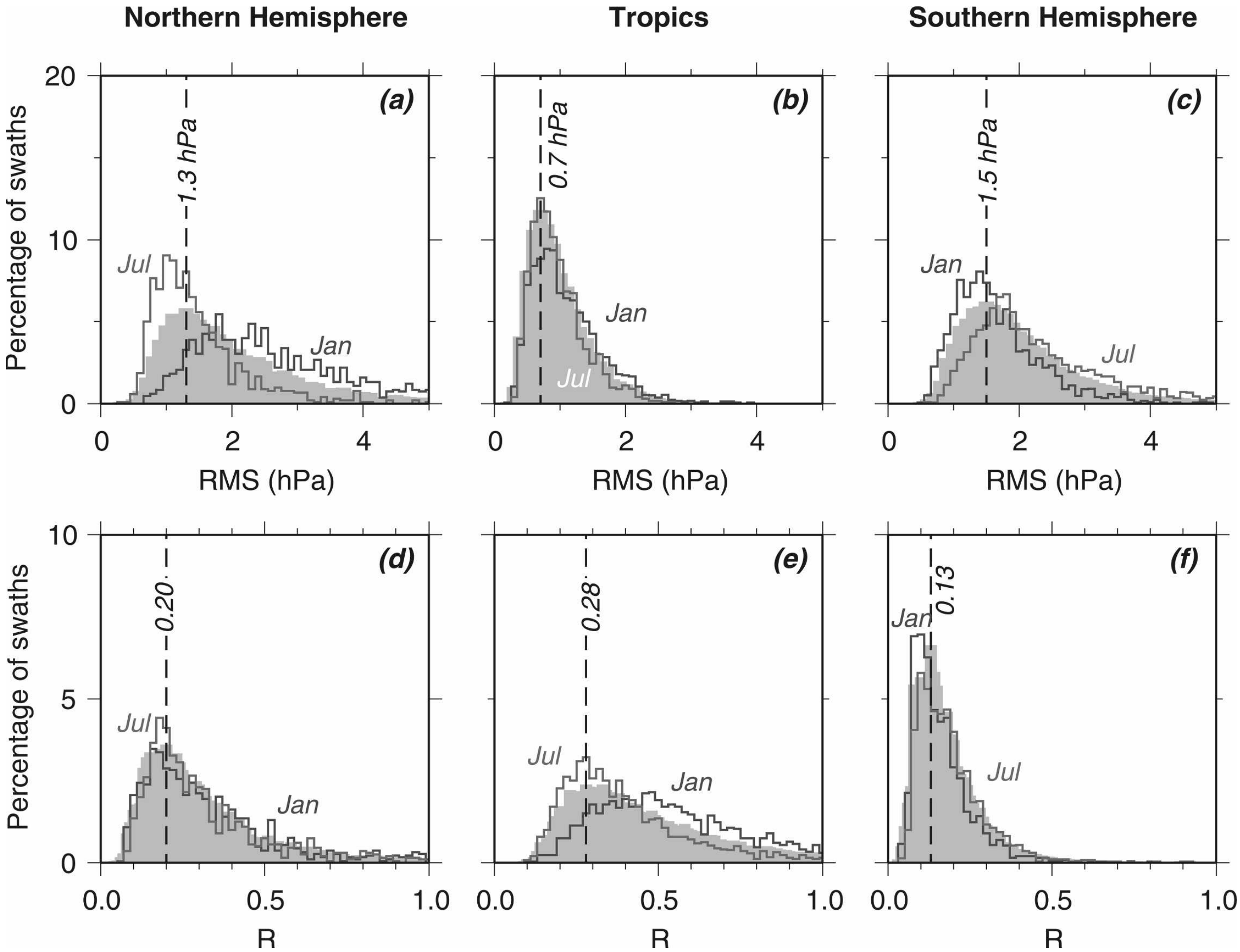

FIG. 6. Distribution of (top) rms differences and (bottom) R between ECMWF and UWQS pressure fields for the global ocean.

midlatitudes, defined here as the 20°–60°N latitude band (rms = 2.4 hPa in Fig. 1), in the tropics (20°S–20°N, rms = 2.2 hPa in Fig. 1), and in the southern midlatitudes (60°–20°S, rms = 1.9 hPa in Fig. 1), after removal of the separate means in each case.

The distribution of rms differences over the 1999–2005 period is shown in Figs. 6a–c. The comparison is restricted to swaths that fall within 1 h of the ECMWF synoptic time. The distribution is skewed to the right with a peak at 1.3 hPa in the Northern Hemisphere, 0.7 hPa in the tropics, and 1.5 hPa in the Southern Hemisphere. Figure 6 also includes the distributions of rms for the summer and winter seasons. The rms differences are larger in the winter and smaller in the summer in both hemispheres. The range of variation from winter to summer is very small in the tropics (0.2-hPa difference between the winter and summer peaks). The smaller rms differences in the tropics (and in the summer in the midlatitudes) are partly explained by the fact that the surface pressure fields vary less in the tropics (or in the summer). This is better seen by dividing the rms differences by the rms variations of the pressure field itself and by calculating a quantity R^2 that is analogous to the coefficient of determination used in statistics to measure the goodness of fit of a least squares regression,

$$R^2 = \frac{\sum_{i=1}^{n} [P_{\mathrm{ECMWF}}(i) - P_{\mathrm{UWQS}}(i)]^2}{\sum_{i=1}^{n} [P_{\mathrm{ECMWF}}(i) - \overline{P_{\mathrm{ECMWF}}}]^2}. \tag{7}$$

A value of $R^2 = 0$ indicates a perfect fit. Note that $1 - R^2$ is more often used, but here our definition will allow us to compare R directly to the rms difference. The resulting distributions of R are shown in Figs. 6d–f. These distributions show that there is a better fit (in a relative sense) in the midlatitudes than in the tropics, and a better fit in the Southern than in the Northern Hemisphere. Although the rms distribution peaks at a

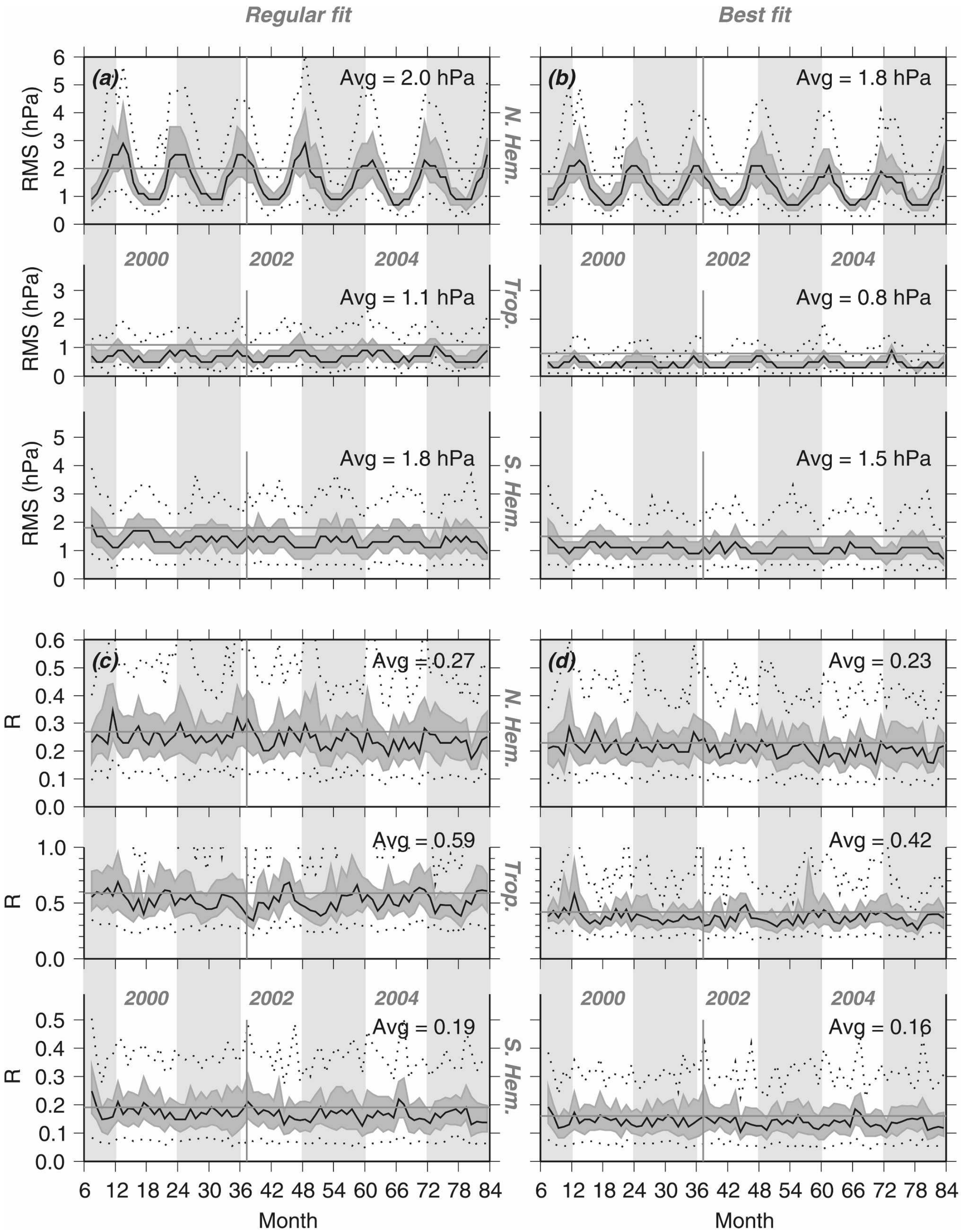

FIG. 7. Temporal variations of the statistics of the rms difference between ECMWF and UWQS pressure fields for the Pacific Ocean: median (black solid line), upper and lower quartile (gray shading), 10th and 90th percentile (dotted lines), and overall mean (gray horizontal line). Shown are (a) rms differences, (b) rms differences after translating the swath and selecting the best fit, (c) R, and (d) R after translating the swath and selecting the best fit. Each panel shows separate statistics for the Northern Hemisphere, tropics, and Southern Hemisphere.

slightly larger value in the Southern Hemisphere than in the Northern Hemisphere (1.5 hPa; Fig. 6c), the range of variations (from 1.4- to 1.8-hPa peak values) is smaller in the Southern Hemisphere than in the Northern Hemisphere (from 1.0 to 1.7 hPa; Fig. 6a).

These results show that ECMWF and UWQS surface pressure fields agree better in an absolute sense, as measured by the rms difference, in the summer (relative to winter) and in the tropics (relative to the midlatitudes). This is at least in part because the pressure fields themselves comprise a narrower range of values in the tropics (relative to the midlatitudes), and in the summer midlatitudes (relative to the winter midlatitudes). However, ECMWF and UWQS agree better in a relative sense, as measured by R, in the midlatitudes (relative to the tropics), and in the Southern Hemisphere (relative to the Northern Hemisphere).

Chelton and Freilich (2005) have shown that the QS surface winds are of sufficiently high quality and consistency over time that they can be used to evaluate the accuracy of ECMWF surface winds. Furthermore, the peaks and widths of the distributions in Fig. 6, combined with the buoy comparisons discussed in section 4, indicate that the UWQS pressures capture both the bulk pressure differences over large distances and the spatial variability of the pressure fields. Because the UWQS pressures are based primarily on the QS winds, this motivates the use of the UWQS pressures as an independent estimator of the surface pressure field, which is consistent over the 7-yr QS period, to investigate the evolution of the ECMWF pressure analyses over that period. Because UWQS pressures use ECMWF SST, T_{air}, and Q_{air} as inputs, they are not entirely independent of changes in the ECMWF analyses over the 7-yr record. However, the pressures depend much more strongly on the QS winds than on the stratification effects. A question of particular interest is whether the agreement between ECMWF and UWQS improves with the assimilation of the QS measurements in the ECMWF NWP model starting on 22 January 2002, as observed in the winds by Chelton and Freilich (2005).

To that end, we calculated monthly statistics of the rms difference over the Pacific Ocean, as shown in Fig. 7a. The calculation is restricted to swaths that fall within 1 h of the ECMWF synoptic time. The variations in the Northern Hemisphere, the tropics, and the Southern Hemisphere are plotted separately. Each panel shows the temporal variations of the median (solid line), the upper and lower quartile (gray shading), and the 10th and 90th percentile. The overall average is shown as a horizontal gray line. The mean and median take on higher values than the peaks shown in

TABLE 2. Mean rms differences and R between the UWQS and ECMWF pressure fields before and after the assimilation of QS winds in the ECMWF NWP model (NH = Northern Hemisphere; SH = Southern Hemisphere). The last difference (italics) is not statistically significant.

	1999–2001	2002–05
	Rms: Regular fit	
NH	2.0	1.9
Tropics	1.0	1.0
SH	1.9	1.8
	Rms: Best fit	
NH	1.8	1.7
Tropics	0.8	0.8
SH	1.6	1.5
	R: Regular fit	
NH	0.27	0.26
Tropics	0.60	0.57
SH	0.19	0.19
	R: Best fit	
NH	0.24	0.23
Tropics	0.43	0.40
SH	*0.16*	*0.15*

Fig. 6 because the distributions are skewed to the right. The rms differences exhibit a clear seasonal cycle around an average of 2.0 hPa in the Northern Hemisphere, 1.1 hPa in the tropics, and 1.8 hPa in the Southern Hemisphere. The variations in the tropics are very small, with a slight tendency to follow those of the Northern Hemisphere. The midlatitude surface pressure differences are larger in the winter and reduced during the summer, although this effect is much larger in the Northern Hemisphere than in the Southern Hemisphere.

Computing the temporal variations of R reduces these contrasts, as shown in Fig. 7c. As pointed out before, R is smaller over the Southern Ocean (0.19, on average) than in the Northern Hemisphere (0.27). In the tropics R is much larger (0.59). The seasonal cycle is much reduced, although the standard deviations remain slightly higher and a seasonal cycle is still apparent in the Northern Hemisphere.

An important contribution to the rms differences between the ECMWF and UWQS pressure fields is due to a simple translation of the weather patterns, even though the structure of the pressure fields themselves might be very similar. It might be caused, for example, by a temporal difference between the synoptic analysis and the satellite pass or by a misplaced storm in the analysis. The UWQS pressure fields are more likely to better capture the position and structure of storm centers than ECMWF. We investigated this effect by recalculating the previous statistics after translating the UWQS pressure fields by ±three grid points (≈±150 km) in the zonal and meridional direction and selecting

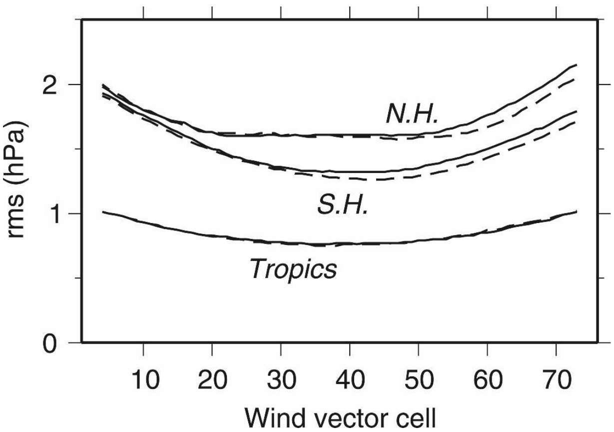

FIG. 8. Rms differences between ECMWF and UWQS pressure fields as a function of cross-swath position, before (solid lines) and after (dashed lines) 22 Jan 2002.

the best fit. The results are shown in the right column of Fig. 7. All statistics are improved, with mean rms differences of 1.8 hPa in the Northern Hemisphere, 0.8 hPa in the tropics, and 1.5 hPa in the Southern Hemisphere.

Two separate statistics are calculated for the periods before and after 22 January 2002, when ECMWF began assimilating QS winds. Because surface pressure is strongly autocorrelated temporally, we sampled scatterometer swaths at 48-h intervals to limit the statistical dependence of the observations (Wilks 2006). The results are summarized in Table 2. The mean rms difference in the midlatitudes decreased by 0.1 hPa after the assimilation of QS winds. The R values also decreased in the Northern Hemisphere and the tropics. All differences in the rms and R values before and after QS assimilation are statistically significant at the 95% level, except for the best fit R in the Southern Hemisphere. Because the UWQS pressure fields can be considered a nearly independent measure of surface pressure, a decrease in the rms difference with the ECMWF surface pressure analyses shows that the assimilation of QS measurements likely had a positive impact on the NWP model. As mentioned in Chelton and Freilich (2005), other changes were implemented in the ECMWF NWP model between 1999 and 2005. However, the respective impacts of these changes, as opposed to the assimilation of scatterometer winds, cannot be disentangled.

The rms statistics are also shown as a function of cross-swath position in Fig. 8, for a subset of swaths in the Pacific Ocean. The figure is to be compared to Fig. 6 in Chelton and Freilich (2005), which shows the speed and direction standard deviations between ECMWF and QS wind vectors as a function of cross-swath position. The wind vector standard deviations are larger at nadir (swath center) and in the outer regions of the swath because of the antenna geometry. Of particular interest in Fig. 8 is the fact that the pressure rms differences are more evenly distributed across the swath, because of the least squares minimization pressure fitting, which tends to distribute the errors throughout the swath. This suggests that a new set of surface wind vectors calculated from the UWQS pressure fields could be in better agreement with the ECMWF surface winds than the original QS winds. This suggests that UWQS pressure fields can be used either as a guide in ambiguity removal, as a filter in the removal of erroneous wind vectors, as a "smoother" in the correction of erroneous wind directions, or as a gap filler in the swath where there is rain contamination. This was demonstrated in Patoux and Brown (2001a) and will be assessed statistically in another article in preparation. The smaller rms differences observed after 22 January 2002 above are also reflected in Fig. 8 (dashed lines).

The asymmetry between the left- and right-hand sides of the swath, before and after 22 January 2002, is due to the presence of land, which sometimes removes large portions of the swath and puts more weight on certain wind vector columns when anchoring the swath to the ECMWF analyses. The asymmetry is partly removed when performing the same analysis on a selected set of swaths far from the coast, although very few swaths are completely unaffected by land and the statistics become noisy (not shown).

6. Spectral analysis

Our third assessment of the UWQS pressure fields is a comparison of their spectral components with those of the ECMWF surface pressure analyses. The spectral characteristics of scatterometer winds have been shown to differ both in total energy and slope from NWP model analyses (Chelton et al. 2006; Milliff et al. 2004, 1999; Wikle et al. 1999; Chin et al. 1998; Freilich and Chelton 1986; Patoux and Brown 2001b). The important conclusion from these spectral analyses is that the scatterometer winds have significantly higher energy at scales of motion smaller than approximately 500–1000 km.

Following Freilich and Chelton (1986) and Patoux and Brown (2001b), we compute the power spectral density on an along- and cross-track grid and assume that the effects resulting from the spherical shape of the earth are negligible. The grid spacing is 50 km and the grid spans 1600 km in both directions, which translates into a wavenumber resolution from 0.000 625 (1600 km) to 0.01 km^{-1} (100 km).

Figures 9a,c shows typical spectra for the southern

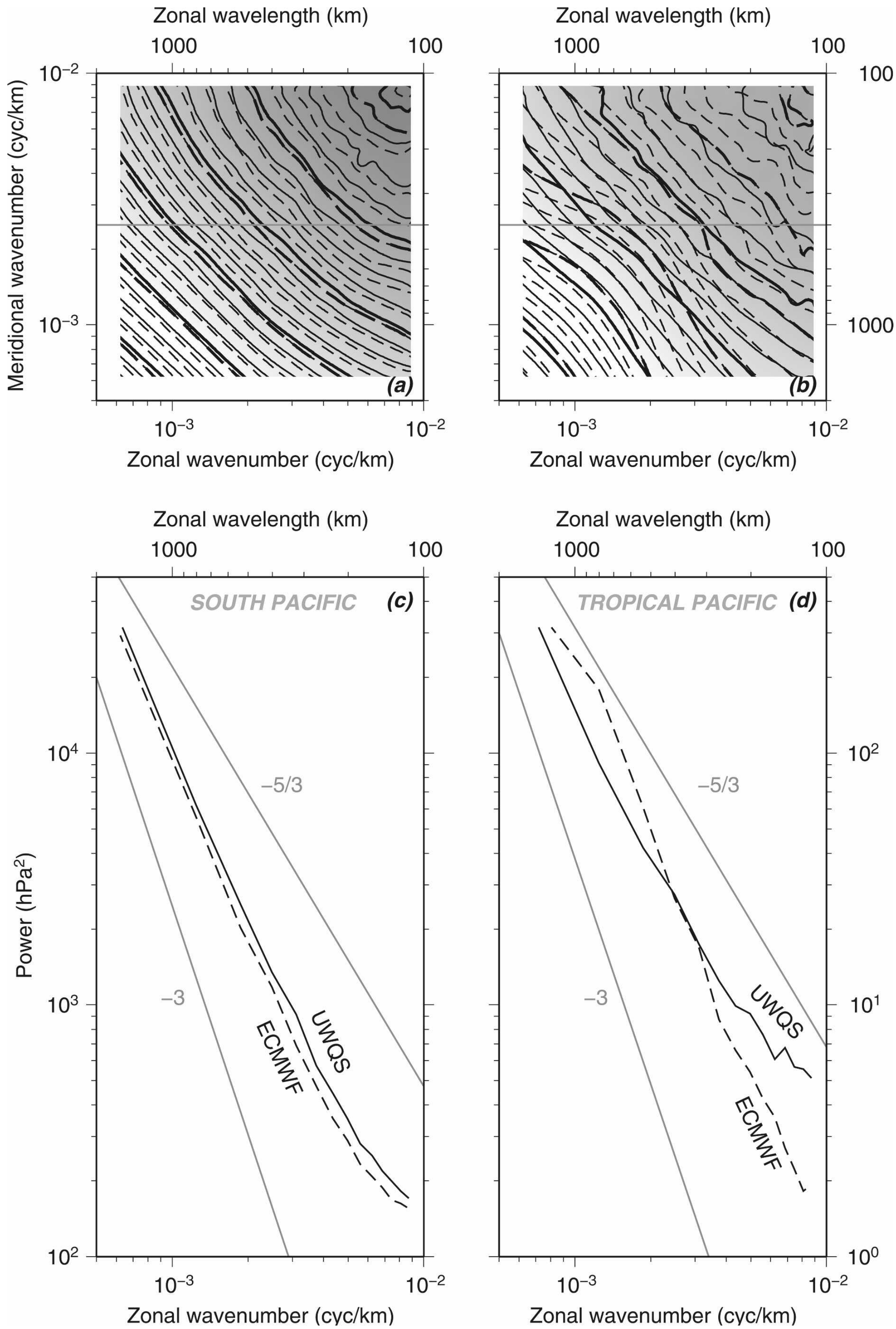

FIG. 9. Spectral decomposition of the UWQS (solid lines) and ECMWF (dashed lines) pressure fields averaged over the (a), (c) southern and (b), (d) tropical Pacific Ocean in May–July 2003. (top) Two-dimensional decomposition. Every fourth line is thicker for comparison. (bottom) Cross section for meridional wavelength 400 km is indicated by the gray line in (a) and (b). The −5/3 and −3 slope are indicated for reference.

Pacific Ocean during austral winter 2003 in which 402 spectra have been computed from 402 ascending swaths and averaged. The grid spans roughly 20° latitude, from 25° to 45°S. We verified the consistency of the results by restricting the decomposition to descending swaths and performing the decomposition at different sampling intervals, by imposing a 2- and 4-day separation between sampled swaths (not shown). Figure 9a shows the two-dimensional decomposition, where frequencies and wavelengths on the x axis correspond to zonal variations in pressure, and to meridional variations on the y axis. The bottom-left part of the spectrum (lighter gray) corresponds to large wavelengths, whereas the top-right corner (darker gray) corresponds to short wavelengths (high frequencies). Figure 9c is a cross section of the two-dimensional spectrum where the meridional wavenumber is held constant at 400 km, as shown by the gray line in Fig. 9a. The $-5/3$ and -3 slopes are indicated for reference.

The most striking feature of this comparison at meridional wavelength 400 km is that the ECMWF and UWQS spectra are very similar, although the UWQS spectrum has more energy at all scales and this difference increases for zonal wavelengths smaller than $\approx$500 km. Similar midlatitude spectra were calculated in regions of the North Pacific, North Atlantic, South Pacific, and South Atlantic Oceans. Although the total energy of the slope varies with the season and the geographical location, these spectra share the same basic characteristics as the spectra shown here and, in particular, do not show systematic differences between the Northern and Southern Hemisphere spectra.

Figures 9b,d show similar decomposition over the tropical Pacific Ocean. The power spectrum indicates more energy at short wavelengths in the UWQS pressure fields than in the ECMWF analyses. It suggests that the UW PBL model might capture more of the mesoscale variability of the surface pressure field in the tropics, through an increased variability of the QS winds themselves. If the QS winds are not fully assimilated in the ECMWF NWP model at the mesoscale, it is likely that the corresponding mesoscale structures will be missing in the surface pressure fields as well, reducing the spectral density at those wavelengths.

However, the power spectrum reveals less energy at scales of 500–1600 km in the UWQS pressure fields, which suggests that the UW PBL model does not capture the full synoptic tropical weather patterns. Future improvements in the characterization of the tropical boundary layer and parameterization of tropical PBL processes in the UW PBL model will specifically address these limitations.

7. Discussion

The three methods for evaluating UWQS sea level pressure demonstrate that the retrieved pressure patterns are of generally high quality and compare well with both in situ buoy data and the ECMWF analyses. Overall, the midlatitude UWQS pressures are in better agreement than those in the tropics, which indicates the need for improvements in this region. Future work will focus on improving the PBL models used for retrieving pressure from surface winds. We intend to merge the separate midlatitude and tropical PBL models into a single PBL model that includes nonlinear momentum advection (Levy 1989; Snyder 1998), baroclinicity (Foster et al. 1999; Bannon and Salem 1995; Levy 1989), secondary circulations (Foster 1996, 2005; Morrison et al. 2005; Brown 1970, 1980; Etling and Brown 1993), variable boundary layer height, and entrainment at the top of the PBL. Such a model will transition smoothly across all latitudes, with the appropriate terms dominating the pressure gradient calculation as we move either into and out of the tropics or midlatitudes, or nearer to or farther from inhomogeneities, such as fronts and storms.

One interesting difference between this study and previous comparisons of QS winds to NWP analyses is that the midlatitude spectral variance of the UWQS and ECMWF pressures are comparable for all resolvable scales. In contrast, the ECMWF surface winds, both before and after ECMWF began to assimilate QS winds, have far too little variance at scales smaller than $\approx$500–1000 km relative to QS (Milliff et al. 2004). One possible explanation for this discrepancy is that the surface wind–to–surface pressure gradient relationship in the 4D variational methods used by ECMWF is much less direct than the relationship in the UW PBL model. The UWQS system seeks an optimal solution for the large-scale forcing (the pressure gradients as modified by PBL turbulence, stratification, etc.) that produced the wind field observed by the scatterometer. The ECMWF analysis seeks the *overall* optimal solution to the entire atmospheric state, not only the surface wind field or surface pressure. Because the surface pressure represents the column weight of the atmosphere, it is closely tied to mass conservation. Thus, the ECMWF surface pressure is constrained by balance conditions with the whole atmosphere, more than by the surface wind field. Consequently, even though the ECMWF surface wind variance in the 500–1000-km wavelengths is underestimated, the ECMWF surface pressure fields do capture the variance at these scales.

The most striking feature of the evaluation presented here is that the Southern Hemisphere rms and R are lower and have a smaller seasonal cycle than those in the Northern Hemisphere. Because the methodology for retrieving pressure from QS winds does not depend on the hemisphere, these differences are real. We examine some possible explanations for this difference here.

There are hemispheric differences in meteorology. The synoptic weather systems in the Southern Hemisphere remain relatively intense all year long. In comparison, the seasonal contrast is stronger in the Northern Hemisphere as midlatitude cyclones give way to the Bermuda high and the Hawaiian high in the summer. However, based on the discussions above, both the UWQS and ECMWF pressure fields resolve the same basic midlatitude structures for scales of 100–1600 km. Consequently, we do not believe that the higher rms is primarily due to seasonal differences between the two hemispheres.

The spectra do not provide information on differences in the locations of storms and fronts. A contribution to the rms differences might be location differences in the weather patterns between ECMWF and UWQS pressure fields. A possible cause mentioned in section 5 is the time differences between the QS swaths and the analyses. However, based on the buoy BPG comparisons and the best-fit calculations shown in Fig. 7, we expect that such location differences are small and that, while this is an important consideration, it is insufficient to explain all of the hemispheric differences in rms.

The ECMWF analysis system incorporates both conventional and remotely sensed observations of the atmosphere with a short-term forecast to find an optimal estimate of the atmospheric state. In the Southern Hemisphere, in situ observations are sparse. Consequently, ECMWF surface pressures can be expected to be more "attuned" to satellite observations, including QS, and therefore in better agreement with scatterometer-derived pressure fields. In the Northern Hemisphere, in situ observations are much denser and the ECMWF surface pressures can be expected to depart from satellite observations in order to accommodate in situ measurements. This is consistent with the lack of a statistically significant difference in midlatitude Southern Hemisphere best-fit R after assimilation of QS winds.

Another potential explanation for the observed differences in the ECMWF and UWQS surface pressure fields can be found in the differences in the surface winds themselves. Chelton and Freilich (2005) found that, relative to QS, there is an overall low bias of about 0.4 m s^{-1} in the ECMWF surface wind analyses. After assimilation of QS winds, both the bias and standard deviation of the difference between QS surface wind speeds and the ECMWF analyses are larger in the winter than in the summer, and the magnitudes of these differences are much larger in the Northern than in the Southern Hemisphere (H. Hersbach 2006, personal communication). The UWQS pressure retrieval is directly related to the QS surface winds, so larger winter and Northern Hemisphere differences in the surface wind could translate into larger differences in pressure. Therefore, larger rms differences point to differences in the representation of the PBL dynamics between the UW and ECMWF PBL models that are largest in the winter and in the Northern Hemisphere.

Spatially isolated regions of large differences between the QS and ECMWF surface winds are not found in the Southern Hemisphere winter, while the largest differences between QS and ECMWF surface winds in the Northern Hemisphere winter are found in specific isolated regions (H. Hersbach 2006, personal communication). SST fields indicate that these regions are near to and over the western boundary currents and their extensions into the midoceans. Consequently, baroclinicity and stratification play major roles in the midlatitude PBL dynamics. O'Neill et al. (2003) and Chelton (2005) have shown that the coupling between the surface winds and SST variations in ECMWF is about half as strong as that observed in the QS vectors. Hence, the full potential impact of QS winds has not been incorporated into the ECMWF analyses. O'Neill et al. (2003) and Chelton (2005) interpret the coupling between SST and U_{10}^{N} as being partly due to the near-surface stratification. For similar conditions, the more unstable the boundary layer, the higher the surface wind and the smaller the frictional turning. In addition, baroclinic shear strongly affects both the speed and turning shear in the PBL (Levy 1989; Bannon and Salem 1995). Foster et al. (1999) demonstrated that PBL baroclinicity modifies NSCAT U_{10}^{N} at least as strongly as stratification (and stronger near fronts). Depending on the sense of the thermal advection, baroclinicity can either enhance or reduce the stratification-induced surface wind modifications.

The winter storm tracks in the Northern Hemisphere encounter stronger zonal temperature gradients than in the Southern Hemisphere (A. Stoffelen 2006, personal communication). Because baroclinicity affects both the surface wind speed and direction, the relationship between the surface winds and pressure gradients can be very different when thermal wind shear is significant. This will change the storm depth and/or location. To test this idea, we reran the pressure retrieval for some selected winter swaths that had relatively high rms differences. In most cases the rms difference was reduced when baroclinicity was included. However, the PBL model failed to estimate pressure gradients for a very small number of vectors, and in some instances the rms difference increased. These results indicate that the UWQS pressure retrievals could be improved by including a thermal wind parameterization.

Limitations of the PBL parameterization and representation of sea surface and air temperature in the ECMWF model most likely contribute to the observed rms differences. Brown et al. (2005) have identified errors in the representation of the PBL structure in the 40-yr ECMWF reanalyses (ERA-40), in particular the underestimation of the wind turning in cases of warm advection. We therefore hypothesize that the higher winter rms differences in the Northern Hemisphere relative to the Southern Hemisphere are most likely due to a combination of effects. Both ECMWF and UWQS pressure fields are estimates of the actual surface pressure from completely different methodologies that have different weaknesses in their boundary layer parameterizations. Apparently these effects tend to occur in the same or nearby regions and where the overall pressure gradients tend to be large. Relatively small location or storm intensity differences can contribute to large rms if they occur in high-gradient regions. The studies of Chelton et al. (2006), Milliff et al. (2004), and Chelton and Freilich (2005) suggest that there may be residual errors in the ECMWF surface pressure analyses that would be largest in the Northern Hemisphere winter locations where the differences between the ECMWF and QS surface winds are largest.

8. Conclusions

In this study the oceanic surface pressure fields computed from QS surface wind vectors using the UW PBL model were evaluated using three methodologies. A comparison with buoy pressure measurements in the North Pacific and North Atlantic Oceans yields a correlation of $R^2 = 0.936$ between buoy and UWQS bulk pressure gradients (BPG) with a slight tendency for the BPG to be overestimated in the UWQS pressure fields (slope $b = 1.014 \pm 0.003$), although the slope varies from a buoy pair to the next.

A computation of the rms difference between UWQS and ECMWF surface pressure fields yields a mean rms difference fluctuating around 2.0 hPa over the northern Pacific Ocean, 1.8 hPa over the southern Pacific Ocean, and 1.1 hPa in the tropics. The computation of the goodness of fit R dampens the seasonal fluctuations and yields a mean R fluctuating around 0.27 over the northern Pacific Ocean, 0.19 over the southern Pacific Ocean, and 0.59 in the tropics. Differences between the Northern and Southern Hemisphere reflect the higher variability in the QS wind measurements observed over the North Atlantic and North Pacific Oceans. The mean rms difference between UWQS and ECMWF pressure fields is smaller after 22 January 2002 in the midlatitudes, which reflects the impact of the assimilation of QS measurements on the ECMWF NWP model.

These rms differences between the UWQS and ECMWF pressure fields are partly due to a translation of the pressure fields. The rms differences and R are reduced by translating the pressure fields by $\pm$three grid points and choosing the best fit. The remaining differences are due to differences in structure between the two surface pressure products. This is also supported by the third analysis, a spectral decomposition of UWQS and ECMWF pressure fields and a comparison of their average spectral components. The analysis shows that the UWQS surface pressure fields contain more energy at all scales in the midlatitudes, with the difference increasing toward smaller wavelengths. However, this difference is not as drastic as the sharp drop-off in ECMWF surface wind variance observed by Milliff et al. (2004). The UWQS spectra reveal less energy at large wavelengths and more energy at small wavelengths in the tropics. We hypothesize that some of the larger rms differences observed in the Northern Hemisphere are due to differences in the parameterization of stratification and baroclinicity in both models.

This three-pronged evaluation of the UWQS pressure fields shows that combining scatterometer surface wind vectors with a PBL model is a powerful way of calculating swath-based surface pressure fields that are consistent with the scatterometer winds and correlate well with buoy measurements. As we improve our model to better capture advective effects in the PBL and entrainment at the top of the PBL, we expect these correlations with buoys to increase. These swath-based pressure fields constitute an almost uninterrupted dataset from July 1999 to the present, and will most likely be interrupted in the near future with the demise of the aging QS scatterometer. We intend to calculate similar pressure fields from the new European Space Agency Advanced Scatterometer (ASCAT) measurements, although some of the advantages offered by QS (such as swath width and higher resolution) will be lost.

This study also suggests that mesoscale information present in the QS winds is not assimilated into the ECMWF analyses. One of our current research projects investigates the possibility of incorporating the mesoscale information contained in the UWQS surface pressure fields into ECMWF global surface analyses using a wavelet-based method similar to that used by Chin et al. (1998) to create global surface wind fields. These *blended* surface pressure fields are used to identify and track low pressure centers, and to determine the extent to which incorporating scatterometer-derived information improves our analysis and understanding of those meteorological features. It points to the need for an improved assimilation of scatterometer information, possibly through the assimilation of scatterometer-derived pressure swaths rather than winds, or through an improvement of the ECMWF PBL scheme to better translate the scatterometer measurements into surface pressure information.

This analysis presents the statistical properties of the UWQS pressure fields. Another important application is the detailed case-by-case analysis of surface pressure fields in the framework of weather forecasting. Near-real-time (NRT) swath-based QS winds are available at the NOAA Ocean Prediction Center (OPC). OPC forecasters use the NRT QS winds to improve the manual surface wind analyses (Chelton et al. 2006). However, using NRT swath winds has not commensurately improved the sea level pressure in the OPC manual analyses, which may be a reflection of the forecasters' reluctance to deviate strongly from the NWP surface pressure (Chelton et al. 2006). The challenge is that the relationship between surface wind and surface pressure is complex and difficult to reconcile in an operational setting. While OPC forecasters have also found that assimilation of scatterometer winds into the NCEP analysis system has had a positive impact, these NWP analyses often underestimate both the maximum surface wind speed and the depth of midlatitude storms. OPC recently implemented the UWQS pressure retrieval scheme in their operational system and have found that it often produces deeper lows than the NWP analyses, improves the location of low pressure centers, and improves the structure of the cyclonic systems. An assessment of the UWQS pressure fields from such an operational point of view, which is complementary to the more climatological analysis presented here, will be reported in the near future.

Acknowledgments. We thank Hans Hersbach for his help in interpreting the comparisons with ECMWF analyses, Ad Stoffelen for reviewing this article and providing insightful comments, three anonymous reviewers for their constructive criticism, and Neal Johnson for his help in creating and maintaining our Web interface to the scatterometer-derived pressure fields. This research was supported by NASA OVWST grant support under JPL Subcontract 1285663.

REFERENCES

Bannon, P. R., and T. L. Salem Jr., 1995: Aspects of the baroclinic boundary layer. *J. Atmos. Sci.,* **52,** 574–596.

Brown, A. R., A. C. M. Beljaars, H. Hersbach, A. Hollingsworth, M. Miller, and D. Vasiljevic, 2005: Wind turning across the marine atmospheric boundary layer. *Quart. J. Roy. Meteor. Soc.,* **131,** 1233–1250.

Brown, R. A., 1970: A secondary flow model for the planetary boundary layer. *J. Atmos. Sci.,* **27,** 742–757.

——, 1980: Longitudinal instabilities and secondary flows in the planetary boundary layer: A review. *Rev. Geophys. Space Phys.,* **18,** 683–697.

——, 1998: Global high wind deficiency in modeling. *Remote Sensing of the Pacific Ocean by Satellites,* R. A. Brown, Ed., Southwood Press, 69–77.

——, 2000: On satellite scatterometer model functions. *J. Geophys. Res.,* **105,** 29 195–29 205.

——, and W. T. Liu, 1982: An operational large-scale marine planetary boundary layer model. *J. Appl. Meteor.,* **21,** 261–269.

——, and G. Levy, 1986: Ocean surface pressure fields from satellite-sensed winds. *Mon. Wea. Rev.,* **114,** 2197–2206.

——, and L. Zeng, 1994: Estimating central pressures of oceanic midlatitude cyclones. *J. Appl. Meteor.,* **33,** 1088–1095.

——, and ——, 2001: Comparison of planetary boundary layer model winds with dropwindsonde observations in tropical cyclones. *J. Appl. Meteor.,* **40,** 1718–1723.

Chelton, D. B., 2005: The impact of SST specification on ECMWF surface wind stress fields in the eastern tropical Pacific. *J. Climate,* **18,** 530–550.

——, and M. H. Freilich, 2005: Scatterometer-based assessment of 10-m wind analyses from the operational ECMWF and NCEP numerical weather prediction models. *Mon. Wea. Rev.,* **133,** 409–429.

——, ——, J. M. Sienkiewicz, and J. M. Von Ahn, 2006: On the use of QuikSCAT scatterometer measurements of surface winds for marine weather prediction. *Mon. Wea. Rev.,* **134,** 2055–2071.

Chin, T. M., R. F. Milliff, and W. G. Large, 1998: Basin-scale, high-wavenumber sea surface wind fields from a multiresolution analysis of scatterometer data. *J. Atmos. Oceanic Technol.,* **15,** 741–763.

Endlich, R. M., 1961: Computation and uses of gradient winds. *Mon. Wea. Rev.,* **89,** 187–191.

Etling, D., and R. A. Brown, 1993: Roll vortices in the planetary boundary layer: A review. *Bound.-Layer Meteor.,* **65,** 215–248.

Foster, R. C., 1996: An analytic model for planetary boundary roll vortices. Ph.D. thesis, University of Washington, 193 pp.

——, 2005: Why rolls are prevalent in the hurricane boundary layer. *J. Atmos. Sci.,* **62,** 2647–2661.

——, and R. A. Brown, 1994: On large-scale PBL modelling: Surface wind and latent heat flux comparisons. *Global Atmos.–Ocean Syst.,* **2,** 199–219.

——, ——, and A. Enloe, 1999: Baroclinic modification of midlatitude marine surface wind vectors observed by the NASA scatterometer. *J. Geophys. Res.,* **104,** 31 225–31 237.

Freilich, M. H., and D. B. Chelton, 1986: Wavenumber spectra of Pacific winds measured by the Seasat scatterometer. *J. Phys. Oceanogr.,* **16,** 741–757.

Harlan, J., Jr., and J. J. O'Brien, 1986: Assimilation of scatterometer winds into surface pressure fields using a variational method. *J. Geophys. Res.,* **91D,** 7816–7836.

Hilburn, K. A., M. A. Bourassa, and J. O'Brien, 2003: Development of scatterometer-derived surface pressures for the Southern Ocean. *J. Geophys. Res.,* **108,** 3244, doi:10.1029/2003JC001772.

Hsu, C. S., and W. T. Liu, 1996: Wind and pressure fields near tropical cyclone Oliver derived from scatterometer observations. *J. Geophys. Res.,* **101D,** 17 021–17 028.

——, M. G. Wurtele, G. F. Cunningham, and P. M. Woiceshyn, 1997: Construction of marine surface pressure fields from scatterometer winds alone. *J. Appl. Meteor.,* **36,** 1249–1261.

Huddleston, J. N., and B. W. Stiles, 2000: A multidimensional histogram rain-flagging technique for seawinds on QuikSCAT. *Proc. IEEE Int. Geoscience and Remote Sensing Symp.,* Vol. 3, Honolulu, HI, IEEE, 1229–1231.

Kalnay, E., and Coauthors, 1996: The NCEP/NCAR 40-Year Reanalysis Project. *Bull. Amer. Meteor. Soc.,* **77,** 437–471.

Kelly, K., S. Dickinson, M. McPhaden, and G. Johnson, 2001: Ocean currents evident in satellite wind data. *Geophys. Res. Lett.,* **28,** 2469–2472.

Levy, G., 1989: Surface dynamics of observed maritime fronts. *J. Atmos. Sci.,* **46,** 1219–1232.

——, and R. A. Brown, 1991: Southern Hemisphere synoptic weather from a satellite scatterometer. *Mon. Wea. Rev.,* **119,** 2803–2813.

Liu, W. T., 2002: Progress in scatterometer application. *J. Oceanogr.,* **58,** 121–136.

Milliff, R. F., W. G. Large, J. Morzel, T. M. Chin, and G. Danabasoglu, 1999: Ocean general circulation model sensitivity to forcing from scatterometer winds. *J. Geophys. Res.,* **104,** 11 337–11 358.

——, M. Freilich, W. Liu, R. Atlas, and W. Large, 2002: Global ocean surface vector wind observations from space. *Observing the Oceans in the 21st Century,* C. J. Koblinsky and N. R. Smith, Eds., GODAE Project Office and Bureau of Meteorology, 102–119.

——, J. Morzel, D. B. Chelton, and M. H. Freilich, 2004: Wind stress curl and wind stress divergence biases from rain effects on QSCAT surface wind retrievals. *J. Atmos. Oceanic Technol.,* **21,** 1216–1231.

Morrison, I., S. Businger, F. Marks, J. Businger, and P. Dodge, 2005: An observational case for the prevalence of roll vortices in the hurricane boundary layer. *J. Atmos. Sci.,* **62,** 2662–2673.

O'Neill, L. W., D. B. Chelton, and S. K. Esbensen, 2003: Observations of SST-induced perturbations of the wind stress field over the Southern Ocean on seasonal time scales. *J. Climate,* **16,** 2340–2354.

Patoux, J., cited 2004: UWPBL 4.0, the University of Washington Planetary Boundary Layer (UWPBL) model. University of Washington. [Available online at http://pbl.atmos.washington.edu/Uwpbl30/home.html.]

——, and R. A. Brown, 2001a: A scheme for improving scatterometer surface wind fields. *J. Geophys. Res.,* **106D,** 23 985–23 994.

——, and ——, 2001b: Spectral analysis of QuikSCAT surface winds and two-dimensional turbulence. *J. Geophys. Res.,* **106D,** 23 995–24 005.

——, and ——, 2002: A gradient wind correction for surface pressure fields retrieved from scatterometer winds. *J. Appl. Meteor.,* **41,** 133–143.

——, R. C. Foster, and R. A. Brown, 2003: Global pressure fields from scatterometer winds. *J. Appl. Meteor.,* **42,** 813–826.

——, G. J. Hakim, and R. A. Brown, 2005: Diagnosis of frontal instabilities over the Southern Ocean. *Mon. Wea. Rev.,* **133,** 863–875.

Snyder, C., 1998: Approximate dynamical equations for fronts modified by the planetary boundary layer. *J. Atmos. Sci.,* **55,** 777–787.

Stevens, B., J. Duan, J. C. McWilliams, M. Münnich, and J. D. Neelin, 2002: Entrainment, Rayleigh friction, and boundary layer winds over the tropical Pacific. *J. Climate,* **15,** 30–44.

Von Ahn, J. M., J. M. Sienkiewicz, and G. M. McFadden, 2006a: The application of sea level pressure and vorticity fields derived from the University of Washington planetary boundary layer model in the NOAA Ocean Prediction Center. *Proc. MTS/IEEE Oceans 2006,* Boston, MA, IEEE, 1–6.

——, ——, and J. Patoux, 2006b: A comparison of sea level pressure analyses derived from QuikSCAT winds to manual surface analyses produced in the NOAA Ocean Prediction Center. *Proc. 21st Conf. on Weather Analysis and Forecasting,* Washington, DC, Amer. Meteor. Soc., 15B.1.

Wikle, C. K., R. F. Milliff, and W. G. Large, 1999: Surface wind variability on spatial scales from 1 to 1000 km observed during TOGA COARE. *J. Atmos. Sci.,* **56,** 2222–2231.

Wilks, D. S., 2006: *Statistical Methods in the Atmospheric Sciences.* 2nd ed. Academic Press, 627 pp.

Zeng, L., and R. A. Brown, 1998: Scatterometer observations at high wind speeds. *J. Appl. Meteor.,* **37,** 1412–1420.

Zierden, D. F., M. A. Bourassa, and J. J. O'Brien, 2000: Cyclone surface pressure fields and frontogenesis from NASA scatterometer (NSCAT) winds. *J. Geophys. Res.,* **105,** 23 967–23 981.